Crater population and resurfacing of the Martian north polar layered deposits

Maria E. Banks,[1,2] Shane Byrne,[1] Kapil Galla,[1] Alfred S. McEwen,[1] Veronica J. Bray,[1] Colin M. Dundas,[1] Kathryn E. Fishbaugh,[2] Kenneth E. Herkenhoff,[3] and Bruce C. Murray[4]

[1] Present-day accumulation in the north polar layered deposits (NPLD) is thought to occur via deposition on the north polar residual cap. Understanding current mass balance in relation to current climate would provide insight into the climatic record of the NPLD. To constrain processes and rates of NPLD resurfacing, a search for craters was conducted using images from the Mars Reconnaissance Orbiter Context Camera. One hundred thirty craters have been identified on the NPLD, 95 of which are located within a region defined to represent recent accumulation. High Resolution Imaging Science Experiment images of craters in this region reveal a morphological sequence of crater degradation that provides a qualitative understanding of processes involved in crater removal. A classification system for these craters was developed based on the amount of apparent degradation and infilling and where possible depth/diameter ratios were determined. The temporal and spatial distribution of crater degradation is interpreted to be close to uniform. Through comparison of the size-frequency distribution of these craters with the expected production function, the craters are interpreted to be an equilibrium population with a crater of diameter D meters having a lifetime of $\sim 30.75 D^{1.14}$ years. Accumulation rates within these craters are estimated at $7.2 D^{-0.14}$ mm/yr, which corresponds to values of ~ 3–4 mm/yr and are much higher than rates thought to apply to the surrounding flat terrain. The current crater population is estimated to have accumulated in the last ~ 20 kyr or less.

1. Introduction

[2] The north polar layered deposits (NPLD) are a multikilometer thick sequence of dusty ice layers (Figure 1a) thought to record previous climatic conditions, much like Earth's ice sheets record terrestrial climate fluctuations in their stratigraphy. Deciphering this polar record has been, and remains today, a major goal of Mars research. Observations by the Mars Reconnaissance Orbiter (MRO) and other recent missions have enabled seminal advances in understanding the polar deposits as relevant to Martian climatic history. We now know that the dust content of the polar deposits is less than a few percent and that internal layers are contiguous across the entire deposit [*Phillips et al.*, 2008]. NPLD accumulation is thought to occur via deposition on the north polar residual cap (NRC) [*Byrne et al.*, 2008]. Understanding the current mass balance of the NRC in relation to the present observed environmental conditions (e.g., atmospheric humidity and surface temperatures) could provide valuable information in linking polar stratigraphy to climate. The NRC is dominated by an approximately decameter-scale texture of light/dark patches [*Thomas et al.*, 2000]. Images with scales as fine as 0.25–0.32 m/pixel from the High Resolution Imaging Science Experiment (HiRISE) aboard MRO [*McEwen et al.*, 2007] show mounds of brighter, finer-grained (i.e., younger) water frost superposing darker, coarser-grained (i.e., older) ice substrate (Figures 1b and 1c). Relief of this texture is likely close to 1 m [*Byrne*, 2009]. Visual and hyperspectral data indicate that the NRC is composed primarily of large-grained, dust-poor (clean) water ice [*Kieffer*, 1990; *Langevin et al.*, 2005].

[3] The length of the geologic record represented by the NPLD remains a central unresolved question. A key piece of information regarding this question is the recent NPLD

---

[1]Lunar and Planetary Laboratory, University of Arizona, Tucson, Arizona, USA.

[2]Now at Center for Earth and Planetary Studies, National Air and Space Museum, Smithsonian Institution, Washington, D. C., USA.

[3]Astrogeology Team, U. S. Geological Survey, Flagstaff, Arizona, USA.

[4]Geological and Planetary Sciences, California Institute of Technology, Pasadena, California, USA.
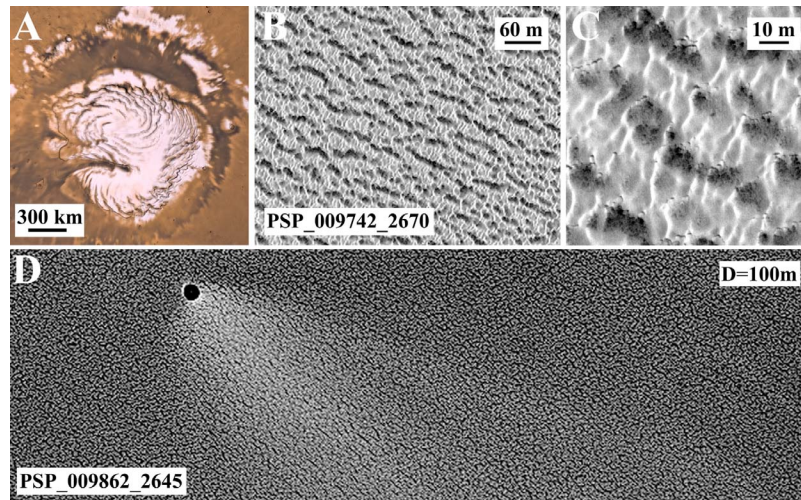
Figure 1. (a) A mosaic of the NPLD as seen by Viking Orbiter 2 (Image credit NASA/JPL/Space Science Institute/USGS). (b and c) Subimages from HiRISE image PSP_009742_2670 of the surface of the NRC showing brighter, finer-grained (i.e., younger) ice superposing darker, coarser-grained (i.e., older) ice (individual dark patches are ~10 m across). (d) HiRISE image PSP_009862_2645 showing a crater with a bright wind streak.

accumulation rate. Layering within the NPLD has been imaged at high-resolution where it is exposed in troughs and scarps. Comparisons of these exposures with models of past orbital change [*Laskar et al.*, 2004] have suggested a link between a ~30 m wavelength periodicity in the stratigraphy to variation of Mars' argument of perihelion (a 51 kyr cycle) [*Laskar et al.*, 2002; *Milkovich and Head*, 2005; *Fishbaugh and Hvidberg*, 2006; *Milkovich et al.*, 2008], although this stratigraphic periodicity remains controversial [e.g., *Perron and Huybers*, 2009] and the exposures themselves may not be characteristic of the internal layering [*Herkenhoff et al.*, 2007]. If the exposures are indeed characteristic of the internal layering, this would imply an average accumulation rate of ~0.5 mm/yr.

[4] Spacecraft constraints on the mass balance of the north polar cap are contradictory. The extent of the NRC varies interannually [*Malin and Edgett*, 2001; *Hale et al.*, 2005]; small changes (~1%) in the area of the NRC seem reversible on time scales of years [*Byrne et al.*, 2008]. While the lack of dust accumulation indicates recent or ongoing accumulation, the exposure of darker, larger-grained ice each year, detected by the Observatoire pour la Minéralogie, l'Eau, les Glaces, et l'Activité (OMEGA), indicates a current net loss of icy material [*Langevin et al.*, 2005]. Small pits observed in HiRISE imagery resemble suncups ~1 m in diameter on the NRC surface and also suggest recent ablation.

[5] Observations by recent missions have helped in developing a better understanding of the stratigraphy laid down by previous climates. However, the climatic conditions themselves and their effect on polar deposition rates can be investigated only with models that lack independent constraints [e.g., *Levrard et al.*, 2007]. Monitoring by various spacecraft over the course of several years has provided a better understanding of the current Martian climate [e.g., *McCleese et al.*, 2008; *Smith*, 2008], yet we still do not know the accumulation rate on the NPLD and the actual connection between polar stratigraphy and climate remains elusive. Thus, understanding the NRC's current mass balance

(the most recent mass balance of the NPLD) is an important step in understanding the climatic record of the NPLD. In this study, we approach this understanding through analysis of the crater population of the NRC.

[6] Populations of impact craters are widely used in planetary science to study surface ages and resurfacing rates. A Viking image search of most of the NRC uncovered no impact craters larger than 300 m, indicating a surface age <100 kyr and a resurfacing rate of at least 1.2 mm/yr [*Herkenhoff and Plaut*, 2000], while *Tanaka* [2005] argued for a surface age of 8.7 kyr based on only two craters known from the limited coverage from the Mars Observer Camera. Images from the Context Camera (CTX) aboard MRO [*Malin et al.*, 2007] now provide complete coverage of the NRC and NPLD at a scale of 6 m/pixel. To better understand and constrain the processes and rates of NRC resurfacing, we conducted a search for craters within the CTX data set. Many craters identified in CTX imagery were re-imaged at higher resolution with HiRISE, revealing a morphological sequence of crater degradation states.

[7] Here we report on our current understanding of the crater population of a region of interest (ROI) defined to represent recently accumulated NPLD and which is mostly coincident with the NRC. The crater size-frequency distribution, as well as the spatial variations in crater degradation, is investigated. The processes involved in crater removal, crater removal rates, and the recent (10–20 kyr) mass balance history of the ROI are discussed in the light of these new constraints. The results of this study indicate that rates of crater degradation and removal are close to uniform both temporally and spatially. The ROI is interpreted to be an equilibrium surface, where craters are removed on a time scale comparable to that over which they accumulate, with a diameter-dependent crater lifetime. Accumulation rates within these polar craters are derived to be an order of magnitude faster than those thought to apply to the NPLD in general.
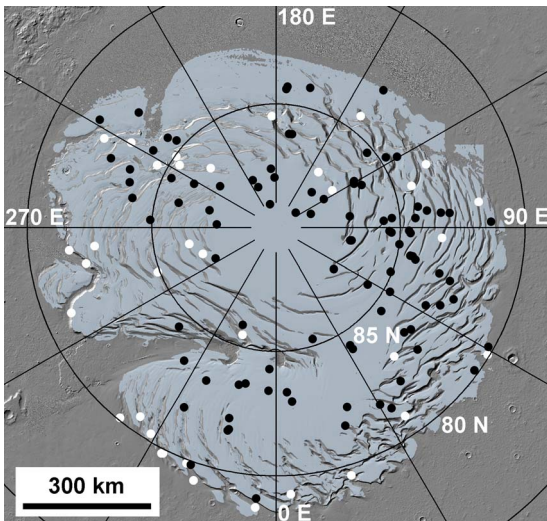
Figure 2. One hundred thirty craters (black and white dots) have been identified and measured on the combined NPLD and NRC with diameters ranging from ~10 to 420 m (excluding outlying craters and craters located in Chasma Boreale). Within the ROI (light gray area), 95 craters (black dots) were identified with diameters ranging from ~10 to 352 m.

[8] This study constrains the crater removal rates. Model results of crater infilling, constrained by the time scales derived in this work, can be applied to modeling accumulation on flat terrain. Analysis of that comparison will be the subject of follow up work.

2. Methods and Data

[9] CTX images were projected using Integrated Software for Imagers and Spectrometers (ISIS) software, and the search for craters within these data was conducted using ArcMap, a component of ESRI's ArcGIS Geographical Information System (GIS). Some craters, especially those imaged in the Northern Hemisphere spring and early summer, were easily located due to bright wind streaks emanating from the crater (Figure 1d). Wind streaks enabled identification of craters as small as ~10 m that otherwise would have been difficult to distinguish because of the texture of the NPLD (Figures 1b and 1c). At the time of this writing, 130 craters have been identified and measured on the NPLD and NRC (excluding outlying craters and craters located in Chasma Boreale) ranging in diameter (D) from ~10 to 470 m (Figure 2). Crater diameters were measured in ArcMap. Several of these craters, occur as clusters of two or more smaller craters that likely formed due to breakup of projectiles in the atmosphere; a single crater equivalent diameter (D_{eff}) was estimated for each cluster using the formula: $D_{eff} = (\sum D_i^3)^{1/3}$ [*Malin et al.*, 2006; *Ivanov et al.*, 2008]. At the time of this writing, HiRISE images have been acquired for 57 of the craters with seven craters imaged in stereo.

[10] Our goal is to investigate the most recent accumulation of the NPLD through examination of the cratering record. To begin, we must determine which areas have most recently accumulated. The NPLD is composed of large flat areas mostly covered with bright, largely dust-free residual ice [*Langevin et al.*, 2005] interspaced with troughs and

scarps that expose its layered interior. While the flat areas are likely sites of recent deposition, the sloping trough walls are not (or else the layered exposures would be covered). In the past, researchers have used the bright residual ice as a proxy for areas of recent accumulation [*Tanaka*, 2005]; however, we now know the residual ice changes in extent by a few percent each year [*Byrne et al.*, 2008] and so in itself is not a reliable proxy of accumulation zones over multiyear time scales. In addition, spectral determination of large grain sizes indicates that the residual ice cap may currently be experiencing a net loss of material each year [*Langevin et al.*, 2005]. We also know the NRC is quite thin, likely decimeters [*Byrne et al.*, 2007], and so craters within patches of residual ice on the surrounding Vastitas Borealis plains do not superpose the residual ice but instead belong to the plains unit. To avoid these issues we describe below an alternate mechanism for isolating the areas of recent accumulation over Planum Boreum used in our analysis.

[11] The 256 pixels-per-degree Mars Orbiter Laser Altimeter (MOLA) digital elevation model (DEM) was used to select our ROI. To begin, a square region (1150 km × 1150 km) containing the topographic dome of Planum Boreum was extracted from the DEM to isolate the general study area. To exclude the low-lying surrounding plains of Vastitas Borealis and the floor of Chasma Boreale, locations below a certain elevation level were excluded; this level varied with longitude as described in Table 1. Outlying deposits of bright polar ice exist but are generally quite thin. It is often difficult to distinguish craters that predate this ice from those that postdate it, so these thin ice deposits were excluded with this elevation criterion.

[12] Terrain covered with dunes was also removed from the ROI. A crater in a dunefield would be rapidly infilled with sand and so the craters (or lack of craters) in these areas would not yield representative NPLD accumulation rates. For this reason, we exclude dunefields by applying a surface roughness cutoff. North polar dunefields have a wavelength that results in aliasing within the MOLA polar DEMs, giving them a highly textured and easily recognizable appearance in shaded relief products. Slopes were calculated from the DEM at one and two pixel wavelengths (230 and 460 m); slopes at longer wavelengths (s2) are expected to be lower than those at shorter wavelengths (s1). The ratio of slopes at these two wavelengths is a measure of how smooth the terrain is and can be reexpressed as a crude estimate of the Hausdorff-Biescovitch dimension [*Turcotte*, 1997] (often referred to as the Hurst exponent), $H = 1 - \log(s2/s1)/\log(0.5)$. The median value of H for the DEM was 0.9; points that had an H value that differed from this median value by more than 0.9 were considered anomalous and excluded. This had the effect of removing dunefields from the ROI.

Table 1. Longitude-Dependent Elevation Values Used in ROI Selection

Longitude Range		Elevation (m)
−180°	0°	−4800
0°	58°	−4500
58°	78°	−4300
78°	88°	−4350
88°	100°	−4400
100°	180°	−4540

[13] Finally, although the ROI contains only dune-free areas of Planum Boreum, we apply one more selection criterion to exclude steeply sloping terrain. Steeply sloping walls of troughs within Planum Boreum experience different amounts of insolation than do flat regions and thus have a very different mass balance history and warrant separate investigation. We exclude any equatorward-facing slopes (with aspect within 90° of south facing) greater than 1° and any poleward-facing slopes (with aspect within 90° of north facing) greater than 7°. These slope cutoffs were also chosen to exclude terrain that displays exposures of internal NPLD layering as such exposures are not sites of recent accumulation.

[14] The ROI resulting from application of these selection criteria is shown in Figure 2 and has an area of 0.7 million km^2. It is a close match to areas covered with residual ice; however, it includes some flat and poleward sloping areas on Planum Boreum currently free of residual ice and excludes some areas of the surrounding Vastitas Borealis unit that do currently have thin covers of residual ice. Within this region, 95 craters were identified with diameters ranging from ~10 to 352 m (Figure 2 and Table 2). Manual inspections of craters less than a kilometer from the margins of the defined ROI were conducted to confirm whether they should be included in the analysis or not; craters were added if they were located on smooth terrain that did not expose layering and excluded if the converse were true.

[15] At the time of this writing, HiRISE images have been acquired for 43 of the 95 craters in the ROI. It should be noted that due to the texture of the NRC, the existence of some of the smaller craters (<25 m) observed in CTX images still needs to be confirmed with HiRISE imagery. At the time of this writing, four of the craters in the ROI have been imaged by HiRISE in stereo. Digital terrain models, at 1 m/post, were produced from HiRISE stereo pairs for two of these craters for detailed topographic analyses. The DEMs were created using the area-based automatic matching package of the commercial stereo software SOCET SET (®BAE Systems) and a preprocessing method developed by *Kirk et al.* [2008]. The vertical precision of the DEMs is ~20 cm [*Kirk et al.*, 2008]. Several of the craters in the ROI occur as clusters of two or more smaller craters; single crater equivalent diameters were determined as described above. In cases where a crater in the ROI was imaged by both HiRISE and CTX, we compared the diameter measurements taken from both data sets (omitting crater clusters) and found that the perceived crater diameter measured in CTX images tended to be a slight overestimate (Figure 3). A linear relation was fit to these data to devise a correction for diameters measured with CTX only (where HiRISE data do not exist).

3. Crater Degradation and Removal

[16] HiRISE observations reveal a continuous morphological sequence of crater degradation states that ranges from craters that are highly degraded to those that are relatively fresh (Figure 4a). These images provide a qualitative understanding of the processes involved in crater removal. The main processes involved in crater degradation and removal appear to be ice accumulation and sublimation, mass wasting, and eolian erosion and deposition. After

crater formation, insolation on the inclined crater walls causes build up of sublimation lag material which eventually slumps into the crater interior. Even the freshest of these craters already shows a sublimation lag on the steep crater walls that appears to be slumping downslope and accumulating on the crater floor (Figure 4a, right). The fact that the remaining bright floor of this particular example is still dust free while the walls are dust-covered argues against significant dust blowing in from the exterior. The interiors of impact craters also appear to be sites of preferential net ice accumulation in that the ice within them is typically brighter than the surrounding NRC; shadowing inside the crater promotes accumulation of fresh, small-grained ice which is brighter, stays cooler, creates a positive accumulation feedback, and eventually infills the crater cavity. Craters can also serve as traps for windblown material (either dust or saltating ice crystals). The bright appearance of the ice infilling these craters indicates that it is both small-grained and low in dust. Some craters that appear to be relatively fresh or young (i.e., little apparent erosion or degradation of crater morphology and a high d/D ratio) have not yet accumulated significant amounts of bright, fresh ice in their interiors (Figure 4a). The pervasive decameter-scale texture of the NRC appears to overprint crater rims leading to their destruction (Figures 1b, 1c, and 4a). Sublimation and eolian erosion also contribute to crater removal by degrading crater rims; wind streaks are observed (Figure 1d) as well as meter-scale ablation pits (suncups) that form on crater walls and the surrounding terrain. The range of morphologies and continuum of states of infill indicate that many craters have likely been removed completely by these processes, a conclusion which the population statistics, discussed in section 4, support. Viscous relaxation is unlikely to have significantly influenced the morphology of these craters due to their relatively small size (most crater diameters are less than 200 m), the relatively short time period involved (less than 20 kyr), and cold (by terrestrial standards) ice temperatures [*Pathare et al.*, 2005].

[17] To better understand and constrain the processes and rates of resurfacing within the ROI, it is necessary to understand the spatial and temporal distribution of crater degradation and removal. Crater depth measurements were acquired from HiRISE DEMs or calculated, where possible, from shadow measurements and used to determine d/D ratios for 13 craters in the ROI (Figure 4b). Most shadow measurements were taken of craters with a flat floor of accumulating ice (i.e., the intermediate stage in Figure 4a) and accurately represent crater depth. Depth/diameter ratios range from 0.03 (mostly infilled) to 0.26 (fresh craters). Among these 13 craters, there is a fairly even distribution of d/D ratios with a slightly larger number of lower d/D ratios (≤0.1) (Figure 4b). Because of the low number of data points (13), the distribution of d/D ratios is interpreted to be uniform. This suggests that crater infill rates have likely been close to constant over the lifetime of the current crater population as a histogram of d/D values is skewed to high/low values when crater infill rates decrease/increase with time.

[18] Because of the limited number of available d/D ratios, we developed a qualitative classification system for HiRISE-imaged craters in the ROI (total of 43 craters) based

Table 2. Craters Identified in the ROI[a]

D (m)	CTX Image ID	HiRISE Image ID	Degradation State[b], d/D Ratio	East Lon	Lat
10[c]	T01_000814_2649_XN_84N231W	PSP_010150_2660	1	116.4	86.1
11	P01_001462_2633_XI_83N266W			88.5	84.6
11	P21_009124_2613_XI_81N288W			64.6	82.7
13	T01_000850_2632_XN_83N127W	ESP_017175_2645[d]		230.3	84.3
16[c]	P02_001688_2617_XI_81N303W	PSP_009929_2605	2	60.6	80.2
18	P01_001509_2637_XN_83N107W	ESP_017108_2640[d]		252.9	83.8
18	P01_001513_2652_XI_85N223W	ESP_017732_2665[d]		119.3	86.4
18[c]	P01_001513_2652_XI_85N223W	ESP_017811_2665[d]		120.8	86.3
18	P01_001583_2646_XN_84N331W			32.1	84.4
18	P21_009071_2652_XI_85N286W			78.0	84.5
19	P22_009440_2660_XN_86N297W			68.7	85.0
21	T01_000874_2695_XI_89N253W			126.8	89.0
22	P01_001510_2650_XN_85N142W	PSP_010529_2630	2	230.0	82.8
23	P01_001607_2646_XN_84N265W	ESP_017285_2645[d]		93.8	84.4
24	P01_001581_2665_XN_86N296W	ESP_017747_2650[d]		82.1	85.0
24	P01_001598_2600_XN_80N004W			355.8	79.1
24	P01_001396_2615_XI_81N259W	ESP_017048_2635[d]		95.1	83.3
25[c]	P01_001607_2646_XN_84N265W	ESP_017786_2655[d]		88.2	85.4
25	P01_001566_2641_XN_84N223W	ESP_017178_2655[d]		129.4	85.2
25	T01_000807_2638_XN_83N035W	ESP_017013_2635[d]		325.6	83.5
25	T01_000810_2641_XN_84N119W			247.2	82.8
25	P01_001601_2668_XN_86N128W	ESP_017055_2665[d]		241.9	86.3
28	P01_001607_2646_XN_84N265W	ESP_017773_2645[d]		98.3	84.2
29	P21_009301_2681_XN_88N149W	PSP_010080_2680	2	206.0	87.9
30	P02_001688_2617_XI_81N303W	ESP_017168_2635[d]		52.9	83.2
30	T01_000832_2649_XN_84N003W	ESP_017091_2645[d]		357.4	84.3
30	P01_001368_2640_XI_84N228W	ESP_017139_2650[d]		122.5	84.7
30	P01_001517_2608_XN_80N317W	ESP_017828_2620[d]		38.9	82.0
30[c]	P01_001607_2646_XN_84N265W	ESP_017839_2640[d]		96.3	83.9
30	P21_009165_2610_XI_81N325W			32.5	81.3
30	P22_009539_2688_XN_88N122W			194.5	89.0
30	T01_000832_2649_XN_84N003W	PSP_010023_2630	1	5.3	82.9
32	P01_001509_2637_XN_83N107W	ESP_017042_2655[d]		244.8	85.3
32	P16_007368_2628_XN_82N219W			142.0	83.0
32	P01_001462_2633_XI_83N266W	PSP_009189_2645	2; 0.10	87.5	84.6
33	P01_001348_2644_XI_84N028W			335.6	83.2
34[c]	P01_001609_2611_XN_81N307W	PSP_008571_2605	1	54.1	80.2
35	P21_009269_2648_XN_84N298W			60.5	84.7
36	P01_001554_2662_XI_86N271W	PSP_009940_2655	3; 0.26	93.4	85.7
37[c]	P21_009071_2652_XI_85N286W			76.9	84.2
37	P01_001456_2685_XI_88N171W	PSP_009528_2680	2	203.9	88.2
38	T01_000823_2642_XN_84N114W	PSP_010027_2640	2	248.2	83.7
38	T01_000859_2643_XN_84N016W	PSP_009918_2635	1	349.0	83.6
39	P02_001670_2643_XN_84N181W	ESP_016463_2645[d]		175.7	84.4
40[c]	P02_001670_2643_XN_84N181W	ESP_017190_2645[d]		175.4	84.3
40	P15_006975_2611_XN_81N284W			72.9	82.7
40	T01_000850_2632_XN_83N127W	ESP_016964_2620[d]		238.5	81.7
40	P01_001388_2670_XI_87N079W	PSP_009749_2670	2; 0.09	233.6	87.2
41	P01_001387_2641_XN_84N019W	PSP_007888_2620	1; 0.06	346.3	82.1
41	P01_001550_2638_XI_83N124W	PSP_009223_2640	2	237.8	84.2
41	P02_001746_2663_XI_86N113W	PSP_009657_2660	2	255.7	86.0
41	P01_001531_2600_XN_80N337W	PSP_010036_2615	3	19.2	81.5
43	P02_001717_2607_XN_80N012W	ESP_017329_2615[d]		346.9	81.6
43	P01_001554_2662_XI_86N271W	PSP_009821_2670	1	80.0	87.0
43	T01_000803_2620_XN_82N280W	PSP_010047_2630	2; 0.16	74.2	83.2
44[c]	T01_000812_2657_XN_85N184W	PSP_009436_2660	2	170.3	86.2

Only craters with diameters of 44.2 m and larger were used to fit the size-frequency distribution and estimate accumulation rates.

D (m)	CTX Image ID	HiRISE Image ID	Degradation State[b], d/D Ratio	East Lon	Lat
45	P01_001388_2670_XI_87N079W			255.6	87.2
45	P01_001516_2619_XN_81N291W	PSP_009955_2625	2	67.9	82.3
48	P22_009576_2589_XI_78N019W			340.3	79.8
48	P01_001554_2662_XI_86N271W	PSP_010006_2655	1; 0.15	94.6	85.3
48	P01_001599_2631_XN_83N039W	PSP_009128_2645	2	315.8	84.4
50	T01_000826_2673_XN_87N236W	ESP_017151_2645[d]		166.3	84.2
50	P01_001388_2670_XI_87N079W	PSP_009761_2675	2	267.1	87.6
51	P01_001420_2682_XI_88N245W			111.1	88.5
52	P21_009417_2641_XI_84N007W			341.3	85.8
52	T01_000812_2657_XN_85N184W	PSP_009001_2660	1	172.1	86.2
53	P01_001561_2630_XN_83N083W	PSP_010158_2650	3	266.6	84.9
54	P01_001609_2611_XN_81N307W	PSP_009982_2625	3; 0.25	49.2	82.5
54	T01_000850_2632_XN_83N127W	ESP_016463_2645[d]		228.7	84.7
55	P21_009263_2675_XN_87N186W			185.0	87.6

Table 2. (continued)

D (m)	CTX Image ID	HiRISE Image ID	Degradation State[b], d/D Ratio	East Lon	Lat
56	P01_001581_2665_XN_86N296W	ESP_016059_2670[d]		54.2	87.1
57	P20_009032_2619_XI_81N293W			62.4	83.2
58[c]	P22_009574_2602_XI_80N328W			30.3	81.7
59	P18_007940_2645_XN_84N005W			357.3	83.4
60	P21_009269_2648_XN_84N298W	PSP_009770_2655	3	58.0	85.6
61	P02_001738_2671_XI_87N266W	PSP_009794_2670	1	98.4	87.0
63	P01_001569_2657_XN_85N317W	PSP_009942_2645	2	51.5	84.6
64	P01_001333_2601_XN_80N335W	ESP_016840_2625[d]		21.6	82.2
64	P22_009793_2671_XN_87N182W			181.6	88.0
65	P01_001583_2646_XN_84N331W	PSP_010180_2645	2	32.2	84.2
69	P01_001570_2655_XN_85N342W	PSP_010154_2655	1	18.1	85.3
71[c]	P01_001522_2635_XN_83N101W	PSP_010172_2640	2	258.4	84.1
72	P01_001583_2646_XN_84N331W			32.1	84.4
73	P02_001717_2607_XN_80N012W	PSP_007967_2615	1	346.6	81.6
81	T01_000832_2649_XN_84N003W			3.7	83.3
81	T01_000859_2643_XN_84N016W	PSP_009404_2635, PSP_010221_2635	2; 0.07	346.7	83.5
90	P01_001379_2680_XI_88N227W	PSP_001406_2680, PSP_001922_2680	1; 0.03	134.4	88.0
99[c]	P01_001379_2680_XI_88N227W	PSP_009792_2720	3	120.6	87.8
102	P21_009071_2652_XN_85N286W	PSP_009862_2645	3; 0.22	77.9	84.4
105	P01_001554_2662_XI_86N271W	PSP_009742_2670, PSP_009821_2670	3	80.2	86.9
131	T01_000829_2614_XN_81N268W	PSP_010086_2615	1	91.5	81.3
148[c]	P01_001414_2620_XI_82N026W	PSP_009655_2620	3; 0.14	333.1	81.9
194	T01_000854_2636_XN_83N236W	PSP_010084_2645, PSP_009689_2645	3; 0.24	120.3	84.4
212	P01_001572_2667_XN_86N054W	PSP_009773_2675	1	297.4	87.3
352	P01_001396_2615_XI_81N259W	PSP_001580_2630, PSP_001462_2630	1; 0.05	94.7	83.0

[a]Where possible, diameters were measured from HiRISE images. Otherwise, diameters are converted CTX measurements (see Figure 3). In several cases, individual craters appear in more than one CTX image; here we list only one example.

[b]1, highly degraded craters (mostly infilled interiors with highly degraded rims); 2, moderately degraded craters (partially infilled interiors and moderately degraded rims); 3, relatively fresh craters (little to no infilling and crater rim degradation) (see Figure 4a).

[c]Crater cluster. Diameter is the single crater equivalent diameter (D_{eff}) as estimated using the formula: $D_{eff} = (\sum D_i^3)^{1/3}$ [Malin et al., 2006; Ivanov et al., 2008].

[d]Note added in proof, new HiRISE confirmation image. Diameter measurements remain the original converted CTX measurements.

on the degree of apparent morphological crater degradation due to infilling and eolian erosion and sublimation of crater rim material. Highly degraded craters (mostly infilled interiors with highly degraded rims) were given a numerical value of 1, while moderately degraded (partially infilled interiors and moderately degraded rims) and relatively fresh craters (little to no infilling and crater rim degradation) were given values of 2 and 3, respectively (Figure 4a and Table 2). As was observed in the distribution of d/D ratios, there is also a fairly uniform distribution of apparent degradation with a slightly lower number of relatively fresh craters (Figure 4b).

[19] To determine the spatial distribution of crater degradation in the ROI, average d/D ratios and apparent degradation were plotted against latitude and longitude (Figures 4c and 4d). Apparent degradation was divided by 13.5 so that the mean apparent degradation matched the mean d/D ratio. Craters at the highest (above 87°) and lowest (below 84°) latitudes appear to be more degraded compared to those at the middle latitudes. Craters also seem to be less degraded between ~30°–90°E and ~210°–270°E longitude. To assess the significance of the d/D variation, we performed an analysis of variance (ANOVA) statistical test, which is a way of splitting the variance of the entire population into variance within subgroups versus variance between groups. Results of this test are reported as an F ratio; a high F ratio indicates the different subgroups are significantly different. Taking the four longitude groups containing at least one d/D measurement we derive an F ratio of 0.783, which (given the number of degrees of freedom in the system) would occur by chance in a uniform distribution 53.3% of the time.

Taking the d/D ratios in the three latitudinal groups, we derive an F ratio of 3.15, which would occur by chance in a uniform distribution 8.7% of the time. So there is no significance to the differences between longitude bins and the significance of the variation between latitude bins is borderline at best (5% is considered the usual cutoff for statistical significance).

[20] Given the small number of measurements we have (13), additional d/D data from stereo imagery to be acquired in the upcoming Mars year could potentially render the latitudinal variation statistically significant. Degradation may be progressing slightly faster at the highest latitudes because of colder temperatures and lower insolation where crater infilling is followed by less subsequent seasonal ablation, and at NRC edges because more water vapor is available from summer-time heating of soil surrounding the NPLD. Degradation could also be related to the location of individual craters relative to troughs or chasmata, although a qualitative comparison of apparent degradation and d/D ratios to crater proximity to such features also did not show any clear patterns.

[21] Despite the variations seen in Figures 4c and 4d, the spatial distribution of crater degradation within the ROI is interpreted to be close to uniform on the basis of the statistical tests described above.

4. Population Statistics

[22] Size-frequency statistics can provide insight into an age for a production surface (a surface where all craters from
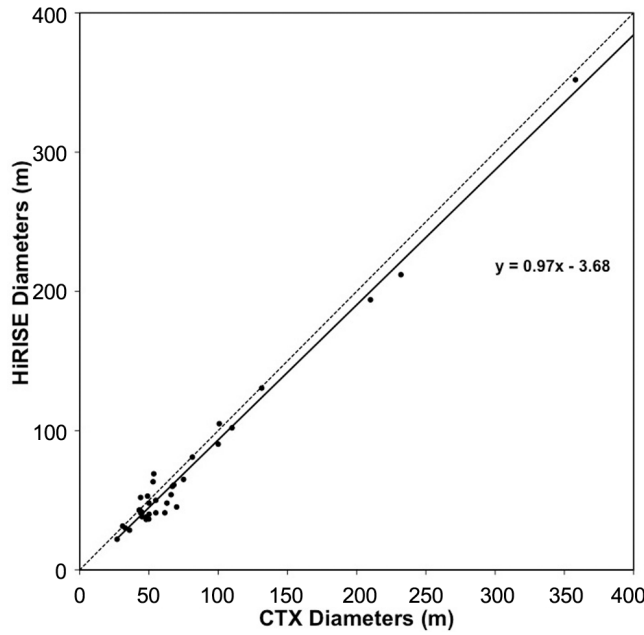
Figure 3. Comparison of diameter measurements for craters measured in both HiRISE and CTX images. Black solid line represents best linear fit.

a certain epoch are recorded) or a crater removal rate for an equilibrium surface (a surface where crater removal balances crater formation). The Martian production function, as predicted from lunar work, is expected to follow a power law where the formation rate of craters of diameter D is proportional to D^{-3} (in the crater diameter range of interest here) [*Hartmann*, 2005] including the effects of atmospheric screening of projectiles [*Popova et al.*, 2003]. Although the slope of *Hartmann*'s [2005] isochrons may be uncertain at low crater diameters, recent small-crater counts on the proximal ejecta lobes of the young Zunil crater found the predictions of this production function to be accurate [*Kreslavsky*, 2008, 2009]. The ROI contains only a sparse population of small craters that must all have been formed recently (we will argue for a time scale of 10–20 kyr below). These craters are all presumed to be primary impacts and not secondaries as no large (multikilometer) craters are known or suspected to have formed elsewhere on Mars to generate secondary impacts in this size range in the recent past. Abundant secondary craters ~100 m in diameter require a nearby primary crater at least 10 km in diameter; a crater this size forms somewhere on Mars about every 10^6 years [*Ivanov*, 2001], so it is unlikely that one formed close to the NPLD in the past ~10^4 years. Furthermore, fields of secondary craters have the same age and should have the same state of degradation, not widely variable preservation as observed within the ROI (assuming spatially uniform degradation rates which the analysis in the previous section supports).
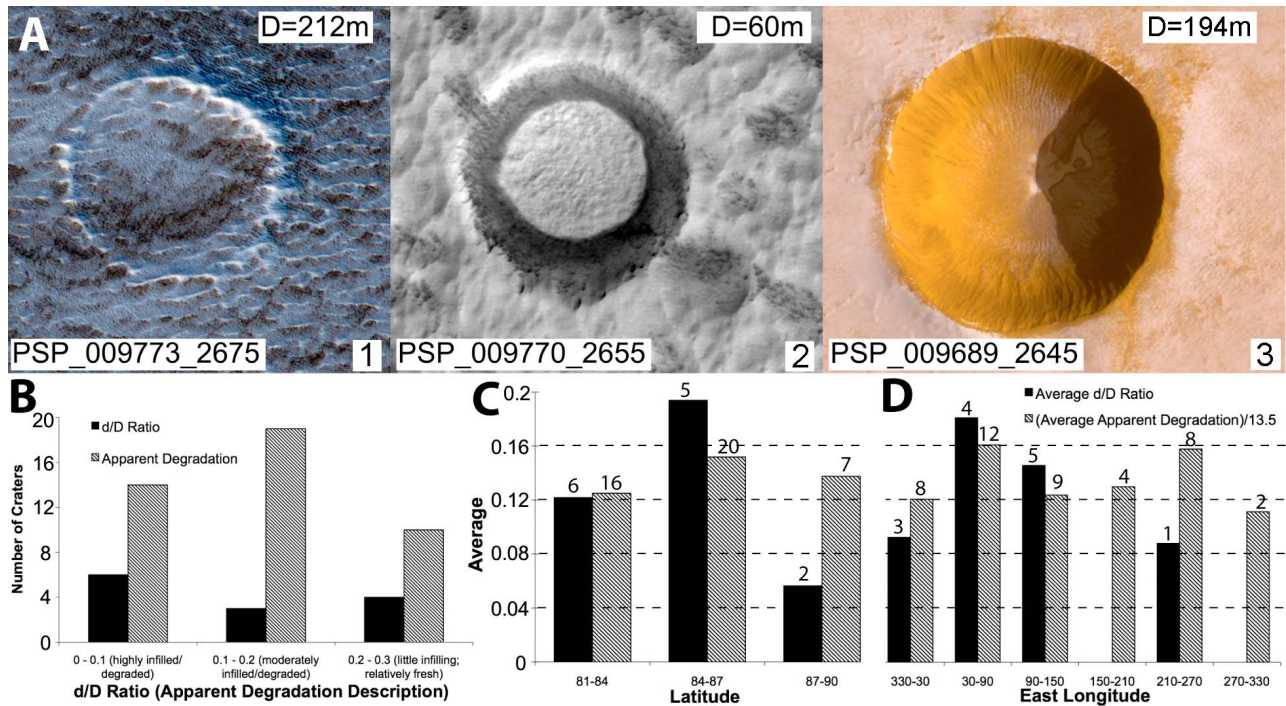
Figure 4. (a) HiRISE images of representative craters from each apparent degradation category (labeled 1 through 3 from most to least degraded). (b) Histogram of the distribution of *d/D* ratios and apparent degradation for HiRISE imaged craters in the ROI. (c) Plot of mean *d/D* ratios and degradation state versus latitude. (d) Plot of mean *d/D* ratios and degradation state versus longitude. For Figures 4c and 4d, apparent degradation was divided by 13.5 so that the mean apparent degradation matched the mean *d/D* ratio.
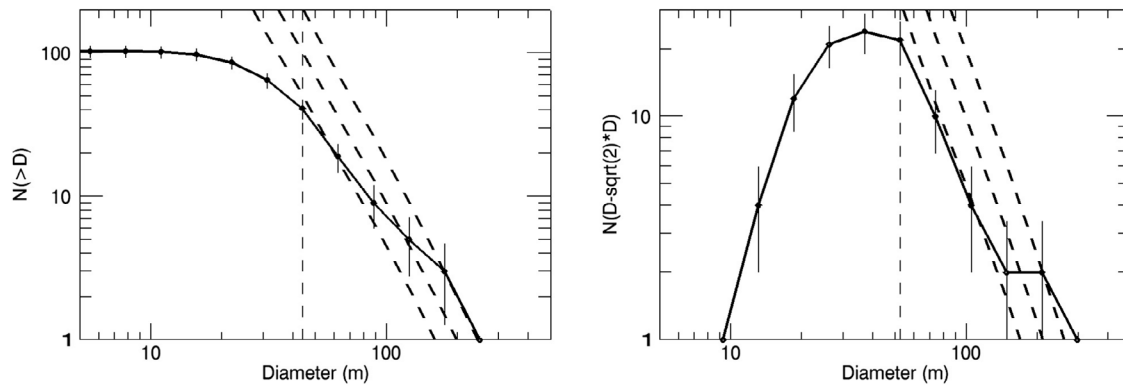
Figure 5. (left) Cumulative and (right) differential size-frequency distribution of craters in the ROI. Bins chosen for the differential plot follow the example of *Hartmann* [2005], with points placed at the bins' geometric centers. For convenience, points on the cumulative-style plot are placed at diameter values that match these bin boundaries. Vertical dashed line shows diameter cutoff below which crater counts are thought to be incomplete. Inclined dashed lines represent (from left to right) 5, 10, and 20 kyr isochrons [*Hartmann*, 2005].

[23] Figure 5 shows the size-frequency statistics of our region of interest plotted both in cumulative and differential form. The bins chosen for the differential plot follow the example of *Hartmann* [2005], i.e., one bin boundary is placed at 1000 m and sequential bin boundaries are separated by a factor of $2^{1/2}$ (which gives the bins a constant width in log-log plots). For convenience, points on the cumulative-style plot are placed at diameter values that match these bin boundaries (although points on the differential plot are placed at the bins' geometric centers). We estimate that our crater counts are complete down to sizes of roughly 35 m based on the expectation that a feature must be several pixels across in the CTX data set (6 m/pixel) to be consistently recognized. A few craters smaller than this were discovered by virtue of large associated wind streaks during the spring (Figure 1d). The low-diameter cutoff is immediately obvious in both plots of the size-frequency statistics (Figure 5). On the basis of the completeness criteria just mentioned and the diameter at which these curves start to roll over, the smallest diameter bin we use for further interpretation is that which starts at 44.2 m. For reasons of statistical robustness, we do not include bins containing only one crater in our analysis (although they are plotted in Figure 5).

[24] It can be seen from Figure 5 that this population of craters, over the diameter range discussed above, does not follow an expected production function (the inclined dashed lines represent the 5, 10, and 20 kyr isochron models of *Hartmann* [2005]). Our crater population is deficient in small craters relative to that expected, i.e., the slope of the size-frequency curve is shallower than the production curve. The slope fit to our size-frequency distribution was −1.89 for the cumulative and −1.85 for the differential plot, whereas a fit to the data tabulated in *Hartmann* [2005] in this diameter range shows the isochron slopes to be −3.04 and −2.99, respectively (this slight mismatch is the result of incorporating atmospheric screening of projectiles which affects the incremental and differential isochrons differently). The observed size-frequency distribution can be explained in terms of an equilibrium population where craters are being removed on a time scale comparable to that

over which they accumulate. In the case of the differential representation, the product of the crater production function (which is diameter dependent) and the crater lifetime (also diameter dependent) creates the size-frequency distribution of craters observed. Taking the fits to the isochrons and size frequency distribution, we find that crater lifetime over the ROI is $30.75D^{1.14}$ years where D is the crater diameter in meters. Thus, for example, a 100 m crater within the ROI is removed in just under 6 kyr.

[25] An equilibrium surface cannot be "dated" with a single age (as the length of time represented by the craters depends on what size of crater you consider). A surface may remain in this equilibrium state for an arbitrarily long period of time; however, we can constrain a minimum amount of time the surface has been in this state by examination of the largest craters. The 212 m diameter crater in the left-hand panel of Figure 4a shows what we consider the most degraded of the large craters (this crater is the second largest in our sample). On the basis of its morphology, we could assume that this crater is so degraded that it is on the verge of being removed. Our above analysis shows that the time needed to remove a 212 m crater such as this is 13.8 kyr, and given its degraded state, this is likely to be only slightly more than the age of the crater itself. The largest crater in our sample (352 m, not shown) is partly infilled. On the basis of its diameter, the crater's estimated lifetime is expected to be 24.6 kyr, and thus the crater formed more recently than this. This crater population contains no information related to preceding epochs. Potential variations in the crater removal rate with location and time, as discussed in the previous section, can complicate these simple interpretations.

[26] Figure 5 also shows a kink in the size-frequency distribution curve at the largest diameters. Because of the low number of craters at these diameters, this kink is not statistically robust; however, it is interesting to note that the points at the largest diameters fall close to the 20 kyr isochron (although within the error bars it could be anywhere from 10 to >20 kyr). It is possible that this surface was cleared of craters as recently as 20 kyr ago or that the resurfacing rate was significantly higher before 20 kyr ago. A

recent study [*Montmessin et al.*, 2007] has argued that when perihelion occurs in the Northern Hemisphere summer, as last happened ~21.5 kyr ago, much icy material may be ablated from the NPLD. Their simulations suggest that several meters of ice may have been removed, which would have been sufficient to remove craters tens of meters in diameter.

[27] There are several uncertainties that must be borne in mind when interpreting these data. The Martian north pole is low in elevation relative to most of Mars so atmospheric effects will be exacerbated beyond that accounted for in the work of *Popova et al.* [2003]. The Martian impact fluxes reported by *Hartmann* [2005] cannot be independently confirmed at this time and may contain errors of unknown magnitude as well. Observations of current cratering on Mars [*Malin et al.*, 2006] have been compared to expected impact fluxes [*Daubar et al.*, 2010; *Hartmann*, 2007]. In the future, there may be enough of these small impacts to independently derive the impactor flux. Also, due to its different mechanical strength and density, an impact into ice may result in a differently sized crater than an identical impact into a rocky target (depending on the temperature of the ice). Additionally, craters in this size range in the lunar mare (where these impact rates are calibrated) form mostly within a loose regolith layer whereas the polar ice in our ROI is likely to be relatively competent. The isochrons plotted on Figure 5 were devised by *Hartmann* [2005] from crater counts of regolith surfaces and thus may not be directly comparable to our crater population. *Senft and Stewart* [2008] examined crater morphologies in terrains on Mars containing icy layers. Their work focused on much larger craters in mixed target material and unfortunately cannot be used here to adjust our crater diameters. Correcting these crater diameters for material properties (perhaps with the use of hydrocode modeling investigations) may result in shifting the size-frequency curve left or right (thus changing the derived crater lifetimes); however the change the slope of the curve is unlikely to be completely explained by this difference (it will likely remain an equilibrium population).

[28] These craters may also expand by sublimation of ice from their steeply inclined walls until a protective sublimation lag builds up. If significant, this process could steepen the size-frequency distribution; we have not quantified the magnitude of this effect and neglect it here in this analysis.

5. Historical Implications

[29] To infer past climatic conditions from the NPLD, we need to connect the current behavior of these deposits to the current climate. However, the resurfacing of Planum Boreum as a whole is not directly equivalent to the crater removal rate as crater interiors appear to be preferred sites for new deposition.

[30] We can constrain the average accumulation rate within craters; knowledge of initial crater depths enables us to derive an accumulation rate if we know the time needed to fill the crater. Here we use the expression for crater lifetime, $30.75D^{1.14}$ (where D is diameter in meters and lifetime is in years), as a simplified approximation for crater infilling time (accumulation within craters is the main way in which they are degraded). An estimate of the initial depth comes from a fresh 194 m diameter crater (Figure 4a) within

our sample. This crater is located in typical NPLD target material and is entirely fresh, with a sharp rim and little accumulated interior ice. The d/D ratio of this crater (calculated from shadow lengths and a HiRISE DEM) is 0.22, within the d/D range of fresh simple craters of 0.2–0.33 [*Melosh*, 1989]. If we assume an initial depth of ~$0.22D$ for all craters in our ROI, then dividing this by the expression for infilling time gives an estimated accumulation rate of $7.2D^{-0.14}$ mm/yr (i.e., accumulation is slightly faster in smaller craters). Over the crater diameter range considered in our statistical analysis, we estimate the average accumulation rate within NPLD craters to be ~3–4 mm/yr. It should be noted that this estimate assumes that the craters are completely filled with ice (d/D ratio of zero) before being removed and does not take into account other crater degradation processes, particularly erosion of raised crater rims, and thus should be considered an upper limit.

[31] The recent accumulation rate of the NPLD is not well known, but several studies have investigated it by comparison of exposed stratigraphy to orbital variations [*Laskar et al.*, 2002; *Milkovich and Head*, 2005; *Fishbaugh and Hvidberg*, 2006; *Milkovich et al.*, 2008]. These studies have argued for an accumulation rate close to 0.5 mm/yr; the accumulation rate we estimate for the interior of NPLD craters is an order of magnitude higher. Our higher estimate is not wholly unexpected as NPLD craters currently appear to be preferential sites of accumulation and this behavior could be expected to persist into the past. Even in craters within areas currently free of residual ice, there is often a bright ice deposit that persists within the crater long after any seasonal frost sublimates. It should also be noted that the accumulation rate we derived within these craters is representative of the past 10–20 kyr while the accumulation rates derived for the NPLD [*Laskar et al.*, 2002; *Milkovich and Head*, 2005; *Fishbaugh and Hvidberg*, 2006; *Milkovitch et al.*, 2008] correspond to the upper ~500 m of material (or ~850 kyr using their accumulation rates). Given the large changes in Martian orbital parameters (and presumably climate) over the latter time scale, it is not surprising that these accumulation rates differ. A recent study by *Chamberlain and Boynton* [2007] shows that midlatitude ground ice has been retreating poleward for the past 10 kyr in response to the increasing argument of perihelion of Mars. This ice is redeposited on the polar cap contributing to the infilling of these craters. The accumulation rate of the NPLD is related to the accumulation rate within these craters although that relationship is probably not straightforward. Future work will investigate what a given crater infill rate means in terms of the accumulation rate for the surrounding flat landscape.

6. Uncertainty From the Largest Size Bin

[32] Examination of the differential plot in Figure 5 shows that straight line fits to the data right of the vertical dashed line are being heavily influenced by the point at 210 m (two craters in the diameter bin 177–250 m). Although we favor retaining this bin in our fits, we could ask how our results would change if that particular bin were excluded and we performed the fit only to the linear portion of the curve. In that case, crater lifetime becomes ~$302D^{0.61}$. The time to remove the degraded 212 m crater in Figure 4a is reduced to

~7.9 kyr and the time needed to remove our largest crater (352 m) is reduced to ~10.8 kyr. In this case, the crater population has been in this equilibrium state for at least ~7.9 kyr and represents less than ~10.8 kyr of history. Accumulation rates within craters are now given by ~$0.73D^{0.39}$ mm/yr (i.e., accumulation is now faster in larger craters). For the craters in our statistically complete diameter range, this corresponds to rates of ~3–7 mm/yr.

[33] Most of these quantities overlap or are within a factor of two of their counterparts in the preceding sections where this size bin (177–250 m) was included. The overall conclusions that these craters represent an equilibrium population and that accumulation within craters is an order of magnitude faster than that thought to occur on the surrounding NPLD remain unaffected though. The main difference resulting from exclusion of craters in this size bin is in the length of time represented by this population, which shrinks from ~20 to ~10 kyr.

7. Summary

[34] To constrain the rate of NPLD accumulation, a search was conducted for craters within CTX images. One hundred thirty craters were identified on the NPLD and NRC (excluding outlying craters and craters located in Chasma Boreale) ranging in diameter from ~10 to 470 m; 95 of the craters are located in a region representing the most recent accumulation and range in diameter from ~10 to 352 m. HiRISE images reveal a morphological sequence of crater degradation that provides a qualitative understanding of the processes involved in crater removal; such processes include ice accumulation, ablation, mass wasting, and eolian processes. For craters in the ROI, d/D ratios were determined where possible (13 craters), and a qualitative classification system for HiRISE-imaged craters (43 craters) was developed based on the degree of apparent crater degradation due to crater infilling and rim degradation. From analysis of the distribution of crater degradation and d/D ratios, crater degradation is interpreted to be close to uniform both temporally and spatially. An analysis of variance test shows that crater d/D ratios do not vary with latitude or longitude in a statistically significant way (although variation with latitude is near the threshold for statistical significance).

[35] Comparison of the size-frequency distribution of these craters with the expected production function shows the ROI to be an equilibrium surface with an estimated crater lifetime of $30.75D^{1.14}$ years (for diameter size bins ranging from 44.2 to 250 m). The current crater population is estimated to have accumulated in the last ~20 kyr or less.

[36] Using a fresh crater within our sample to estimate an initial d/D ratio, we derive the accumulation rates within craters located in the ROI to be ~$7.2D^{-0.14}$ mm/yr, which correspond to estimated values of ~3–4 mm/yr (for craters within the statistically complete diameter range). This is an order of magnitude higher than what is thought to be the geologically recent accumulation rate over the NPLD (0.5 mm/yr) [*Laskar et al.*, 2002; *Milkovich and Head*, 2005; *Fishbaugh and Hvidberg*, 2006; *Milkovich et al.*, 2008]. This comparison is complicated by the fact that these craters are preferential sites for ice deposition (and so should have a higher accumulation rate) and that the two accumulation rates are averages over radically different time scales.

[37] Craters make useful control features as their initial shape, if typical, is very well known and their obliteration rate constrains rates of degradational processes. The full range of crater morphologies observed in HiRISE images allows "space-for-time" substitution and will allow us to model crater degradation in detail. Variations in the argument of perihelion will have affected polar climate over the lifetime of these craters. In future studies, recent orbital solutions [*Laskar et al.*, 2004] will be combined with processes of crater degradation and removal (i.e., accumulation, sublimation, mass wasting, and eolian erosion and deposition of icy material), to create landscape evolution models that are constrained by the size-frequency distribution and the distribution of degradation in the observed crater population discussed in this study. Such models will enable further quantitative investigation of the recent (10–20 kyr) mass balance history of the NPLD. The results of this study are an important initial step in developing an understanding of the NPLD's current behavior and mass balance in relation to the current north polar climate of Mars, and contribute to the long-term goal of inferring Martian climatic history through stratigraphic analysis of the polar layered deposits.

References

Byrne, S. (2009), The polar deposits of Mars, *Annu. Rev. Earth Planet. Sci.*, *37*, 535–560, doi:10.1146/annurev.earth.031208.100101.

Byrne, S., K. E. Herkenhoff, P. Russell, C. Hansen, A. McEwen, and The HiRISE Team (2007), Preliminary HiRISE polar geology results, *Lunar Planet. Sci. Conf.*, *38*, 1930.

Byrne, S., M. T. Zuber, and G. A. Neumann (2008), Interannual and seasonal behavior of Martian residual ice-cap albedo, *Planet. Space Sci.*, *54*(2), 194–211.

Chamberlain, M. A., and W. V. Boynton (2007), Response of Martian ground ice to orbit-induced climate change, *J. Geophys. Res.*, *112*, E06009, doi:10.1029/2006JE002801.

Daubar, I. J., A. S. McEwen, S. Byrne, C. M. Dundas, M. Kennedy, and B. A. Ivanov (2010), The current Martian cratering rate, *Lunar Planet. Sci. Conf.*, 1978.

Fishbaugh, K. E., and C. S. Hvidberg (2006), Martian north polar layered deposits stratigraphy: Implications for accumulation rates and flow, *J. Geophys. Res.*, *111*, E06012, doi:10.1029/2005JE002571.

Hale, A. S., D. B. Bass, and L. K. Tamppari (2005), Monitoring the perennial Martian northern polar cap with MGS MOC, *Icarus*, *174*, 502–512.

Hartmann, W. K. (2005), Martian cratering 8: Isochron refinement and the chronology of Mars, *Icarus*, *174*, 294–320.

Hartmann, W. K. (2007), Martian cratering 9: Toward resolution of the controversy about small craters, *Icarus*, *189*, 274–278.

Herkenhoff, K. E., and J. J. Plaut (2000), Surface ages and resurfacing rates of the polar layered deposits on Mars, *Icarus*, *144*, 243–253.

Herkenhoff, K. E., S. Byrne, P. S. Russell, K. E. Fishbaugh, and A. S. McEwen (2007), Meter-scale morphology of the north polar region of Mars, *Science*, 1711–1715, doi:10.1126/science.1143544.

Ivanov, B. A. (2001), Mars/Moon cratering rate ratio estimates, *Space Sci. Rev.*, *96*, 87–104.

Ivanov, B. A., H. J. Melosh, A. S. McEwen, and the Hirise Team (2008), Small impact crater clusters in high-resolution HiRISE images, *Lunar Planet. Sci. Conf.*, *39*, 1221.

Kieffer, H. H. (1990), H2O grain size and the amount of dust in Mars' residual north polar cap, *J. Geophys. Res.*, *95*(B2), 1481–1493, doi:10.1029/JB095iB02p01481.

Kirk, R. L., et al. (2008), Ultrahigh resolution topographic mapping of Mars with MRO HiRISE stereo images: Meter-scale slopes of candidate Phoenix landing sites, *J. Geophys. Res.*, *113*, E00A24, doi:10.1029/2007JE003000.

Kreslavsky, M. A. (2008), Young populations of small impact craters on Mars as observed in HiRISE images, *AGU*, Abstract P41B-1361.

Kreslavsky, M. A. (2009), Dynamic landscapes at high latitudes on Mars: Constraints from populations of small craters [CDROM], *Lunar Planet. Sci. Conf.*, *40*, 2311.

Langevin, Y., F. Poulet, J. P. Bibring, B. Schmitt, S. Doute, and B. Gondet (2005), Summer evolution of the north polar cap of Mars as observed by OMEGA/Mars Express, *Science*, *307*, 1581, doi:10.1126/science.1109438.

Laskar, J. A., A. C. M. Correia, M. Gastineau, F. Joutel, B. Levrard, and P. Robutel (2004), Long term evolution and chaotic diffusion of the insolation quantities of Mars, *Icarus*, *170*(2), 343–364.

Laskar, J., B. Levrard, and J. F. Mustard (2002), Orbital forcing of the Martian polar layered deposits, *Nature*, *419*, 375–77.

Levrard, B., F. Forget, F. Montmessin, and J. Laskar (2007), Recent formation and evolution of northern Martian polar layered deposits as inferred from a global climate model, *J. Geophys. Res.*, *112*, E06012, doi:10.1029/2006JE002772.

Malin, M. C., and K. S. Edgett (2001), Mars Global Surveyor Mars Orbiter Camera: Interplanetary cruise through primary mission, *J. Geophys. Res.*, *106*(E10), 23,429–23,570, doi:10.1029/2000JE001455.

Malin, M. C., K. S. Edgett, L. V. Posiolova, S. M. McColley, and E. Z. N. Dobrea (2006), Present-day impact cratering rate and contemporary gully activity on Mars, *Science*, 1573–1577, doi:10.1126/science.1135156.

Malin, M. C., et al. (2007), Context Camera Investigation on board the Mars Reconnaissance Orbiter, *J. Geophys. Res.*, *112*, E05S04, doi:10.1029/2006JE002808.

McCleese, D. J., et al. (2008), Intense polar temperature inversion in the middle atmosphere on Mars, *Nat. Geosci.*, *1*, 745–749.

McEwen, A. S., et al. (2007), Mars Reconnaissance Orbiter's High Resolution Imaging Science Experiment (HiRISE), *J. Geophys. Res.*, *112*, E05S02, doi:10.1029/2005JE002605.

Melosh, H. J. (1989), *Impact Cratering: A Geologic Process*, Oxford University Press, 245 pp.

Milkovich, S. M., and J. W. Head III (2005), North polar cap of Mars: Polar layered deposit characterization and identification of a fundamental climate signal, *J. Geophys. Res.*, *110*, E01005, doi:10.1029/2004JE002349.

Milkovich, S. M., J. W. Head, G. Neukum, and the HRSC Team (2008), Stratigraphic analysis of the northern polar layered deposits of Mars: Implications for recent climate history, *Planet. Space Sci.*, *56*, 266–288.

Montmessin, F., R. M. Haberle, F. Forget, Y. Langevin, R. T. Clancy, and J.-P. Bibring (2007), On the origin of perennial water ice at the south pole of Mars: A precession-controlled mechanism?, *J. Geophys. Res.*, *112*, E08S17, doi:10.1029/2007JE002902.

Pathare, A. V., D. A. Paige, and E. Turtle (2005), Viscous relaxation of craters within the Martian south polar layered deposits, *Icarus*, *174*(2), 396–418.

Perron, J. T., and P. Huybers (2009), Is there an orbital signal in the polar layered deposits on Mars?, *Geology*, *37*(2), 155–159.

Phillips, R. J., et al. (2008), Mars north polar deposits: stratigraphy, age, and geodynamic response, *Science*, *320*, 1182–1185.

Popova, O., I. Nemtchinov, and W. K. Hartmann (2003), Bolides in the present and past Martian atmosphere and effects on cratering processes, *Meteorit. Planet. Sci.*, *38*, 905–925.

Senft, L. E., and S. T. Stewart (2008), Impact crater formation in icy layered terrains on Mars, *Meteorit. Planet. Sci.*, *43*(12), 1993–2013.

Smith, M. E. (2008), Spacecraft observations of the Martian atmosphere, *Annu. Rev. Earth Planet. Sci.*, *36*, 191–219.

Tanaka, K. L. (2005), Geology and insolation-driven climatic history of Amazonian north polar materials on Mars, *Nature*, *437*, 991–994.

Thomas, P. C., et al. (2000), North-south geological differences between the residual polar caps on Mars, *Nature*, *404*, 161–164.

Turcotte, D. L. (1997), *Fractals and Chaos in Geology and Geophysics*, 2nd ed., Cambridge Univ. Press, Cambridge.

M. E. Banks and K. E. Fishbaugh, Center for Earth and Planetary Studies, National Air and Space Museum, Smithsonian Institution, MRC 315 PO Box 37012, 4th and Independence, SW, Washington, DC 20013-7012, USA.

V. J. Bray, S. Byrne, C. M. Dundas, K. Galla, and A. S. McEwen, Lunar and Planetary Laboratory, University of Arizona, 1629 E. University Blvd., Tucson, AZ 85721, USA. (shane@lpl.arizona.edu)

K. E. Herkenhoff, Astrogeology Team, U. S. Geological Survey, 2255 N. Gemini Dr., Flagstaff, AZ 86001, USA.

B. C. Murray, Geological and Planetary Sciences, California Institute of Technology, MC 170-25, 1200 E. California Blvd., Pasadena, CA 91125, USA.